

Temperature and thickness dependence of the thermal conductivity in 2D ferromagnet Fe_3GeTe_2

Marcel S. Claro,^{*,†} Javier Corral-Sertal,[†] Adolfo O. Fumega,[‡] Santiago

Blanco-Canosa,^{¶,§} Manuel Suárez-Rodríguez,^{||} Luis E. Hueso,^{||,§} Victor

Pardo,^{*,⊥,♯} and Francisco Rivadulla[†]

[†]*CiQUS, Centro Singular de Investigacion en Quimica Bioloxica e Materiais Moleculares, Departamento de Quimica-Fisica, Universidade de Santiago de Compostela, 15782-Santiago de Compostela, Spain.*

[‡]*Department of Applied Physics, Aalto University, FI-00076 Aalto, Finland*

[¶]*Donostia International Physics Center (DIPC), 20018 San Sebastián, Spain*

[§]*IKERBASQUE, Basque Foundation for Science, Bilbao, Spain*

^{||}*CIC nanoGUNE BRTA, Donostia-San Sebastián, Spain*

[⊥]*Departamento de Física Aplicada, Universidade de Santiago de Compostela, E-15782 Santiago de Compostela, Spain*

[#]*Instituto de Materiais iMATUS, Universidade de Santiago de Compostela, E-15782 Campus Sur s/n, Santiago de Compostela, Spain*

E-mail: marcel.santos@usc.es; victor.pardo@usc.es

Abstract

The emergence of symmetry-breaking orders such as ferromagnetism and the weak interlayer bonding in van der Waals materials, offers a unique platform to engineer novel heterostructures and tune transport properties like thermal conductivity. Here, we report the experimental and theoretical study of the cross-plane thermal conductivity,

κ_{\perp} , of the van der Waals 2D ferromagnet Fe_3GeTe_2 . We observe a non-monotonic increase of κ_{\perp} with the thickness and a large suppression in artificially-stacked layers, indicating a diffusive transport regime with ballistic contributions. These results are supported by the theoretical analyses of the accumulated thermal conductivity, which show an important contribution of phonons with mean free paths between 10 and 200 nm. Moreover, our experiments show a reduction of the κ_{\perp} in the low-temperature ferromagnetic phase occurring at the magnetic transition. The calculations show that this reduction in κ_{\perp} is associated with a decrease in the group velocities of the acoustic phonons and an increase in the phonon-phonon scattering of the Raman modes that couple to the magnetic phase. These results demonstrate the potential of van der Waals ferromagnets for thermal transport engineering.

The electric-field control of the conductivity of atomic-thick graphene^{1,2}, shortly afterwards extended to NbSe_2 and MoS_2 ³, opened up new possibilities for materials properties manipulation in the novel world of 2D van der Waals (vdW) materials and heterostructures⁴. Particularly, on vdW materials, the extreme bonding anisotropy is translated into a giant anisotropy also in the thermal transport, where the in-plane thermal conductivity κ_{\parallel} is much larger than the cross-plane one κ_{\perp} ,⁵ despite the prediction of phonon mean-free paths (mfp) of the order of several tens of nanometers across the weakly bonded planes^{6,7}. Defects and imperfect layer stacking result in a mixed contribution of ballistic transport (large mfp, coherent phonons) and diffusive transport (small mfp), which reduces very much the thermal conductivity across the 2D planes.^{6,8}

A particularly interesting 2D material regarding heat dissipation is the itinerant ferromagnet Fe_3GeTe_2 (FGT): charge doping through Li^+ -intercalation modulates its magnetic anisotropy and increases T_C up to room temperature,⁹ while a strong spin-phonon coupling¹⁰ produces a significant effect of magnetic ordering on the thermal conductivity, opening the door to gate-tunable 2D thermal devices. First-principles calculations in other 2D magnetic materials, like 2H-VSe₂, CrI₃, FeX₃ and RuX₃ (X=Cl, Br, I)¹¹⁻¹⁴, have predicted a large change of the thermal conductivity in their magnetically ordered phase as well, although an

experimental confirmation of such a large switching of the thermal conductivity associated to magnetic ordering in 2D materials is lacking.

In this work, we report experimental measurements combined with a theoretical analysis of the thickness and temperature dependence of the thermal conductivity in FGT. We have observed a non-monotonic increase of the cross-plane thermal conductivity with thickness, characteristic of a mixed ballistic propagation of long mfp phonons with diffusive transport, as well as a large drop of the thermal conductivity in the magnetically ordered phase. Both effects can be understood by our *ab initio* analysis of the thermal conductivity based on density functional theory (DFT) calculations. We also show that artificial layer stacking is a very effective way of blocking the cross-plane thermal transport in FGT.

Results and Discussion

FGT is a 2D itinerant ferromagnet with $T_C \approx 200$ K, which decreases with the number of layers, but retains the magnetic order down to the single-layer limit.¹⁵ Neutron diffraction data support a ferromagnetic (FM) order also along the c-axis¹⁶, although theoretical calculations and analysis of experimental magnetic susceptibility, suggested an antiferromagnetic (AF) stacking below $T_C \approx 152$ K¹⁷. From the structural point of view, the material is weakly bonded off the plane via van der Waals interactions, which facilitates its mechanical exfoliation and transfer of few-layer thick flakes to a substrate. The unit cell consists of two vdW planes with hexagonal symmetry, each formed by 3 Fe atomic planes (see Fig. 1).

The crystals for this study were obtained from hq-graphene (hqgraphene.com; see the X-ray powder diffraction data in Figure S1 in the supplementary information). DC magnetization data of bulk crystals show that $T_C \approx 200$ K, as expected for fully stoichiometric crystals (Figure 2a). Temperature-dependent X-ray analysis shows a change in the slope of the c-axis parameter at T_C (Figure 2b), but no change in the space group of the crystal.

Few-layer thick flakes of FGT were prepared by mechanical exfoliation and transferred

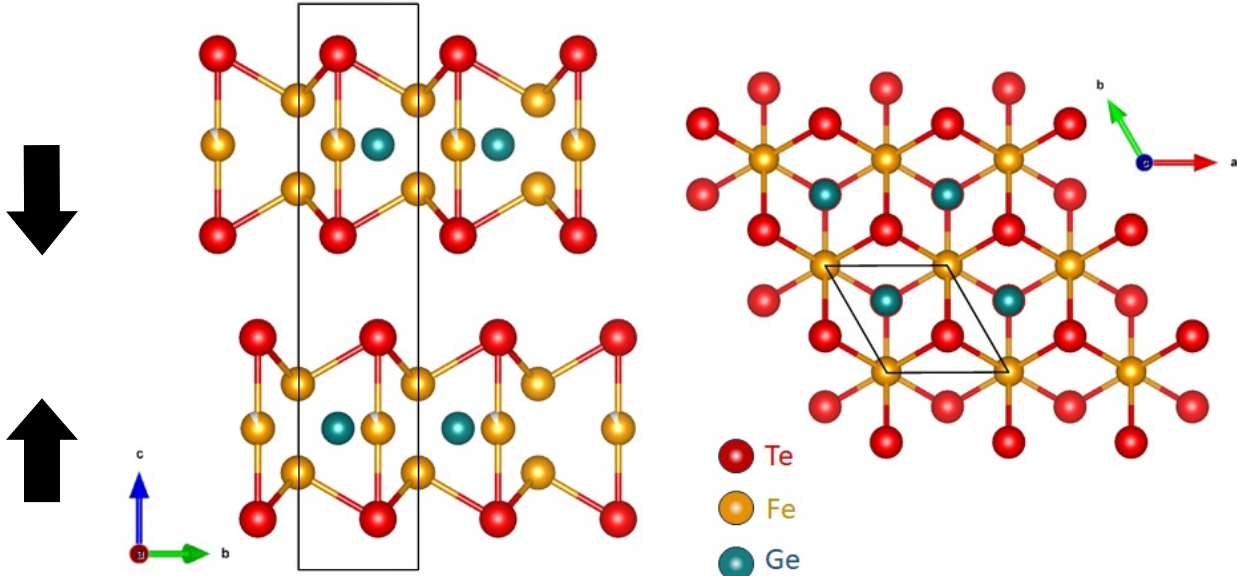


Figure 1: Crystal structure of Fe_3GeTe_2 : a) lateral view of the structure. The cell is formed by two layers, shifted with respect to each other. In the low temperature magnetic phase the layers become ferromagnetic (FM) with an antiferromagnetic interlayer coupling. b) Top view of the structure showing the hexagonal symmetry of the ab plane. Fe, Ge and Te atoms are shown in gold, purple and green, respectively.

to (0001) sapphire substrates, using PDMS stamping¹⁸. Transferred FGT flakes have tens of microns in lateral dimensions and thicknesses ranging from 15 nm to 250 nm (Figure 2 c,d). The flakes are always thicker than 5 layers, considered to be the border between 2D and 3D magnetism,¹⁹ so that the comparison with the bulk calculations is justified. Since vdW materials present high anisotropy between the conductivity in-plane κ_{\parallel} (κ_{xx} , κ_{yy}) and cross-plane κ_{\perp} (κ_{zz}), their values will be considered separately.

Thermal conductivity was measured by Frequency Domain Thermoreflectance (FDTR), using a \approx 60 nm thick layer of Au as a transducer²⁰. To extract κ and the TBC from the FDTR phase-shift curves we fitted the most common model wherein total energy conservation and energy transfer between layers are imposed by a transfer matrix, as explained elsewhere²¹. To reduce the number of fitting parameters, the thickness of the Au layer was measured by X-ray reflectivity, and its thermal conductivity was estimated from the sheet electrical resistance measured by van der Paaw method, and the Wiedemann Franz law. The

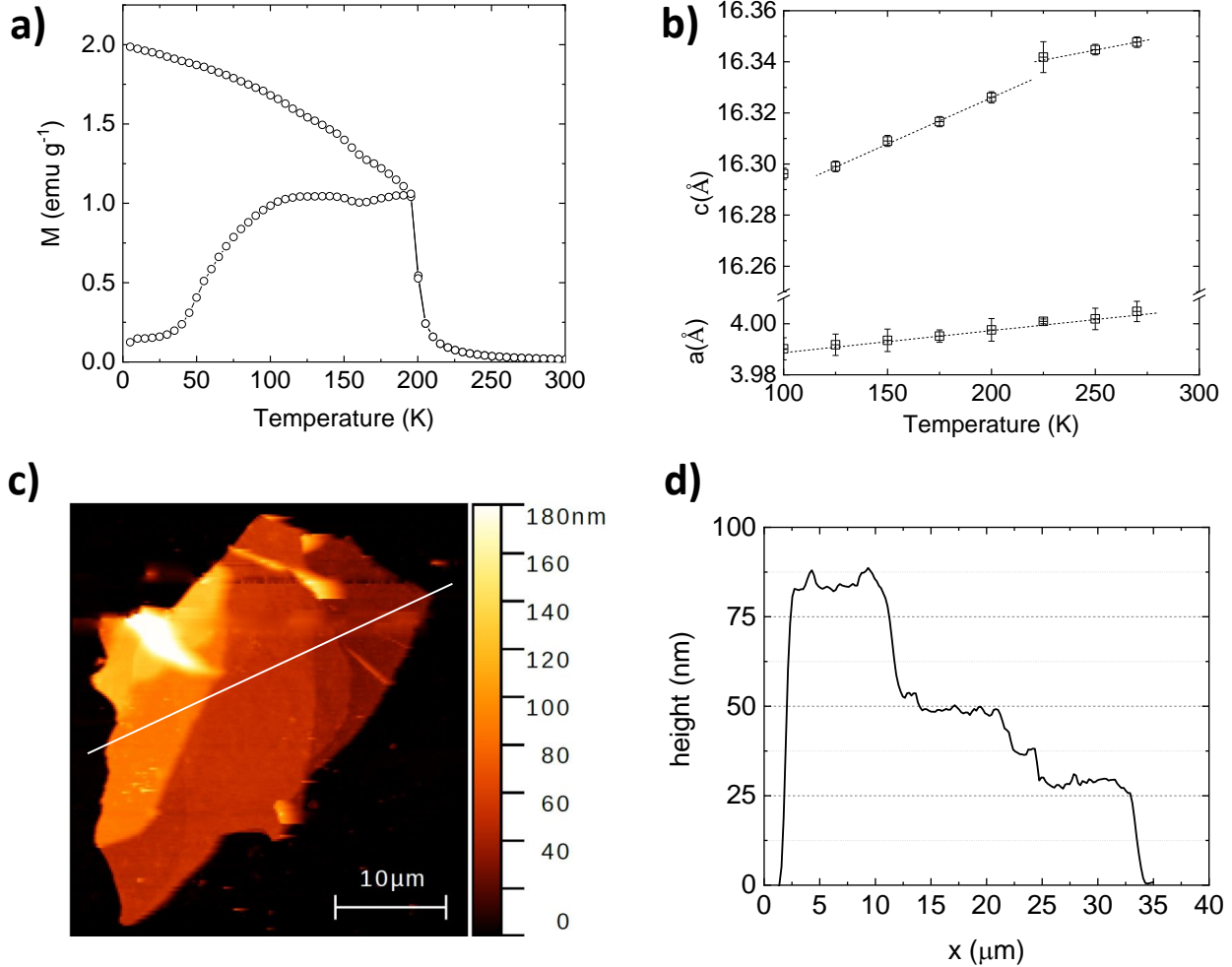


Figure 2: Temperature dependence of the magnetization, a), and lattice parameters, b), measured for a bulk crystal of FGT. c) Atomic force microscopy (AFM) image of one flake transferred to the surface of a (0001) sapphire substrate. The corresponding height profile along the line in c) is shown in panel d).

thickness of the FGT flakes was measured by atomic force microscopy (AFM). Heat capacities were taken from the literature and kept fixed for each temperature in all fittings.²² The thermal conductivity of the substrate was measured and confirmed with the values from the literature.²³ In this way, the free parameters in the fittings are reduced to κ_{\perp} of FGT (we observed that the sensitivity to κ_{\parallel} is very low, and it has a negligible influence in κ_{\perp}), and the TBC between Au/FGT, G1, and between FGT/Al₂O₃, G2. We considered the initial values for G1 $\approx 30\text{-}40$ MWm⁻²K⁻¹, similar to Au/MoS₂⁶, and G2 ≈ 25 MWm⁻²K⁻¹, as reported for MoS₂/Al₂O₃²⁴, and MoS₂/SiO₂⁶ interfaces.

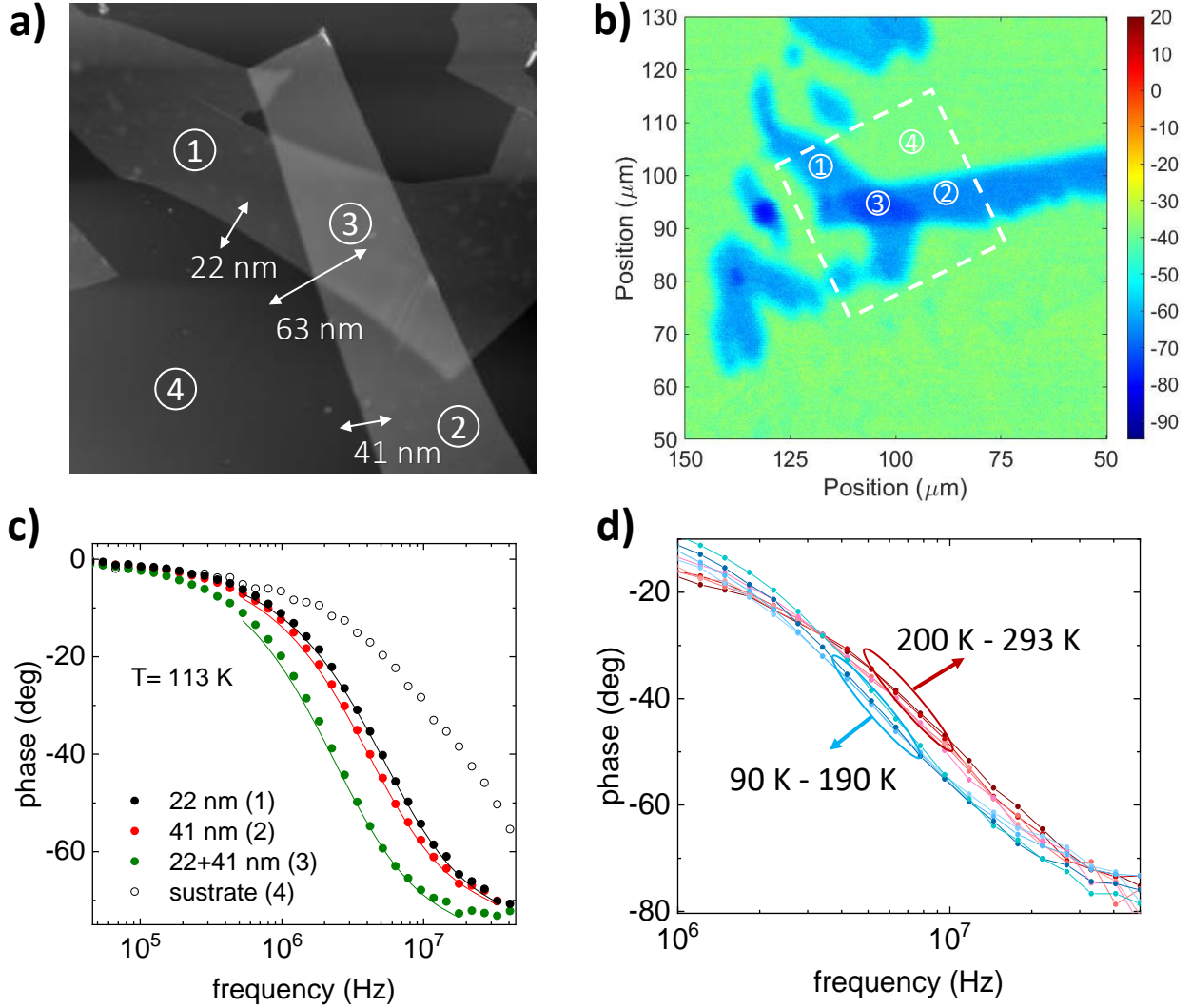


Figure 3: a) $30 \times 30 \mu\text{m}$ AFM topography of two partially overlapping flakes . b) Phase-shift map at 20 MHz of the same region (enclosed within the square) observed in a), with the corresponding points marked. In this image, the flakes are already covered with 60 nm of Au for FDTR measurements. c) Phase-shift vs frequency curves for the three points marked in a) and b), along with the fitting to the thermal model. The curve of the substrate, as a reference, is also shown. d) Phase-shift vs frequency curves of point 2 at different temperatures. There is a large change around 200 K, associated to the magnetic ordering temperature (see text).

On the other hand, the variability of G_2 between mechanically transferred flakes may be an important source of error. For that reason, multilayer flakes like those shown in the Fig. 2 c) are important to reduce problems associated with the variability of G_2 , as they allow the measurement of κ_{\perp} for different thicknesses, with the same FGT/sapphire interface.

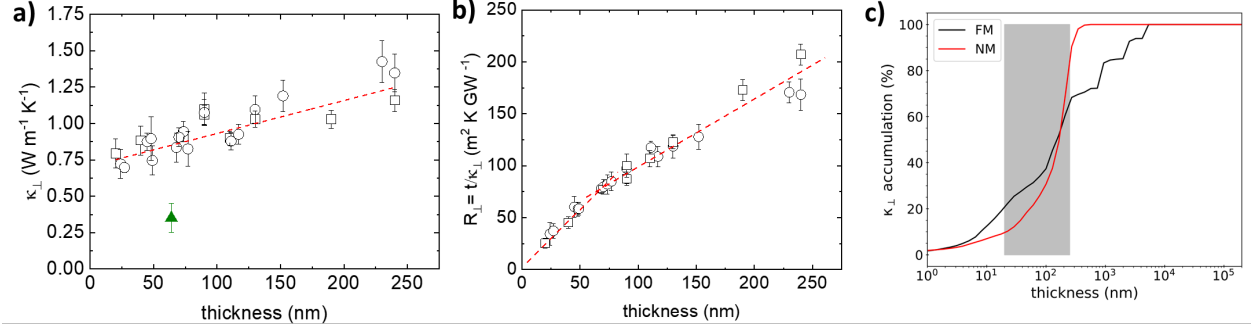


Figure 4: Measured thermal conductivity a), and thermal resistance $R_{\perp}=t/\kappa_{\perp}$, b) at room temperature for different flakes with varying thicknesses. Circles and squares correspond to different sets of crystals, transferred to different substrates. The green solid triangle in a) corresponds to κ_{\perp} at point 3 in Fig. 3a), the region of superposition of the two flakes. The dotted lines are linear fittings. c) Accumulated κ_{\perp} as a function of the phonon mean free path, at 300 K. The shaded area shows the thickness range of the flakes studied by FDTR in this work.

Initial values of κ_{\perp} of 1 W m⁻¹ K⁻¹, typical for other 2D materials, were used for an estimation of the sensitivity to different parameters in different frequency ranges. The spot size was varied between a $1/e^2$ diameter $\approx 4\mu\text{m}$ and $11\mu\text{m}$, for achieving better sensitivity to TBC and κ_{\perp} . The fittings shown in Fig. 3c) to obtain the κ_{\perp} and TBCs reported in this work were performed from 1 MHz to 50 MHz, where the sensitivity for these parameters is maximum (see Figure S2 on Supplementary Information).

Figure 3 a) shows the AFM topography of two partially overlapping flakes of thickness 22 nm and 41 nm each. The $100 \times 100 \mu\text{m}$ phase shift map at 20 MHz shows the variations in the contrast due to the differences in κ_{\perp} and TBC. The whole frequency phase-shift spectra for each point marked in a) and b) are presented in Figure 3 c-d) at different temperatures, demonstrating good sensitivity to thickness and temperature.

The thickness dependence of κ_{\perp} at room temperature is shown in Figure 4a). There is an increase of κ_{\perp} with the thickness of the sample, of the order of ≈ 0.5 W/m K in a range of ≈ 200 nm. Although small, this is of the same order of magnitude as that reported for other van der Waals materials, like MoS₂⁶ or SnSe₂,²⁵ and it is consistent with our DFT calculations; Figure 4c). The calculated accumulated κ_{\perp} , shows that more than 50% of

the heat at 300 K is carried by phonons with a mean-free path larger than ≈ 200 nm, suggesting an important contribution from ballistic phonons along the c-axis, as in other vdW structures^{6,26}.

In the case of pure ballistic transport, phonons can propagate without thermal resistance inside the material, so that $R_{\perp} = R_{int} + t/\kappa_{\perp}$ should be a constant, independent of thickness. However, the measured experimental cross-plane thermal resistance, R_{\perp} , also increases with the thickness (Figure 4b). On the other hand, in a purely diffusive regime, $R_{\perp}(t)$ is linear with constant slope $= 1/\kappa_{\perp}$.⁸ For FGT, R_{\perp} increases linearly with thickness above ≈ 60 nm, giving $\kappa_{\perp} \approx 1.9(1)$ W m⁻¹ K and $R_{int} \approx 46$ m² K/GW, but it deviates from this behavior for thinner samples, with a vanishing resistance as $t \rightarrow 0$. The change in slope suggests some thickness-dependent contribution, and although the data in Figure 4b) seem to extrapolate to zero, the thinner samples measured in this work are $t \approx 25$ nm, so we cannot exclude a small finite value of R_{\perp} close to the monolayer limit (note that a residual value as small as ≈ 10 m² K/GW has been reported for a few monolayers of MoS₂).⁶

We also measured κ_{\perp} in the superposition region of two crystals, point 3 in Figure 3a): κ_{\perp} is substantially reduced in the overlapping region of total thickness 63 nm (green triangle in Figure 4a). Actually, the phase-shift curve of point 3 can be fitted with two layers, of 22 and 41 nm each, with their corresponding κ_{\perp} , and a very high interlayer thermal resistance between both flakes of ≈ 180 m² K/GW (TBC ≈ 10 -12 MW m⁻² K⁻¹). This supports the contribution of phonons with a mfp larger than the thickness of the individual layers, evidencing the mixed contribution of diffusive and ballistic phonons to κ_{\perp} in FGT.

It is also remarkable that the value of the TBC between the two FGT flakes is of the same order of magnitude as reported for interfaces between dissimilar 2D materials, like graphene/MoS₂ or MoS₂/WSe₂,²⁷ although in this case, the large interfacial resistance occurs between films of the same composition, without any mass-density or compositional mismatch. We have neither observed any dependence of TBC nor κ_{\perp} on the relative orientation of the superposed FGT flakes.

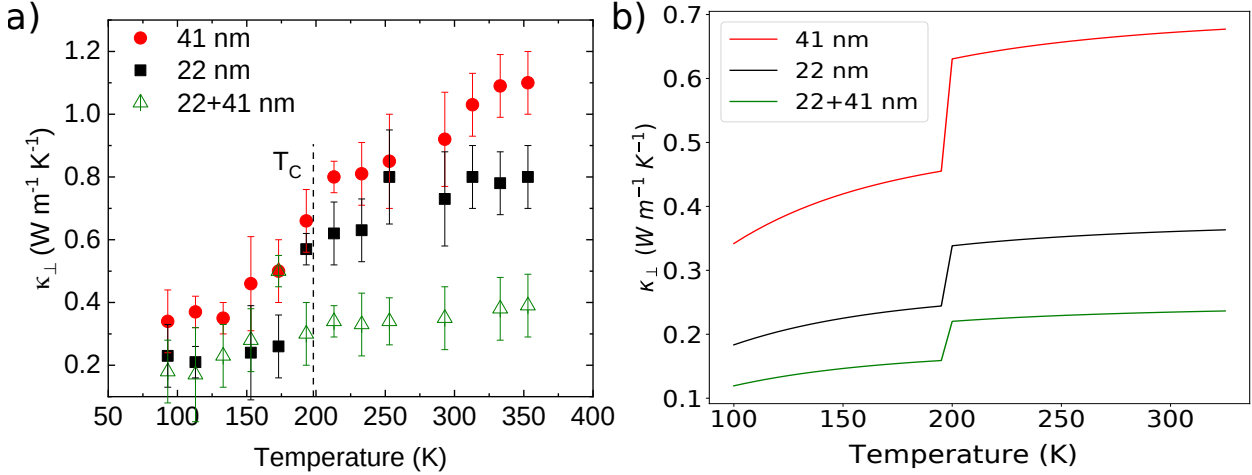


Figure 5: Experimental a) and theoretical b) temperature dependence of the thermal conductivity of two flakes with thicknesses 22 nm, 41 nm and the superposition of both 22+41 nm, corresponding to points 1, 2 and 3 in Fig. 3a) respectively.

Finally, the experimental temperature dependence of κ_{\perp} is shown in Fig. 5a), for two different thicknesses (points 1 and 2 in Fig. 3a). A reduction of κ_{\perp} between 25% and 65% occurs below T_C in the transition to the magnetic phase. Note that the jump in κ_{\perp} is clearly observed in the raw phase-shift curves (Fig. 3d) and therefore it cannot be attributed to fitting artifacts. The temperature dependence of κ_{\perp} in the region of superposition of the two flakes (point 3 in Figure 3a) is also shown. In this case, κ_{\perp} remains very small, with a weak temperature dependence in the whole interval, without any substantial change around T_C , suggesting that in this case the flakes act as independent resistances.

It is common in magnetic and ferroelectric materials that the formation of domain walls causes a reduction of thermal conductivity due to phonon scattering on domain boundaries^{28,29}. However, the κ_{\perp} obtained is robust to external magnetic fields up to 50 mT, applied with a strong toroidal permanent magnet (see Suppl. Information Figure S4 and S5). Based on previous reports³⁰ this applied field should be enough to switch between stripe domains and uniformly magnetized states; the negligible effect of the magnetic field on κ_{\perp} indicates that the in-plane magnetic domains are not the cause of the sudden change of κ_{\perp} at T_c . We have also discarded as a cause of the jump on κ_{\perp} the eventual changes in the crystal structure, since the powder X-Ray diffraction of the original bulk crystal revealed

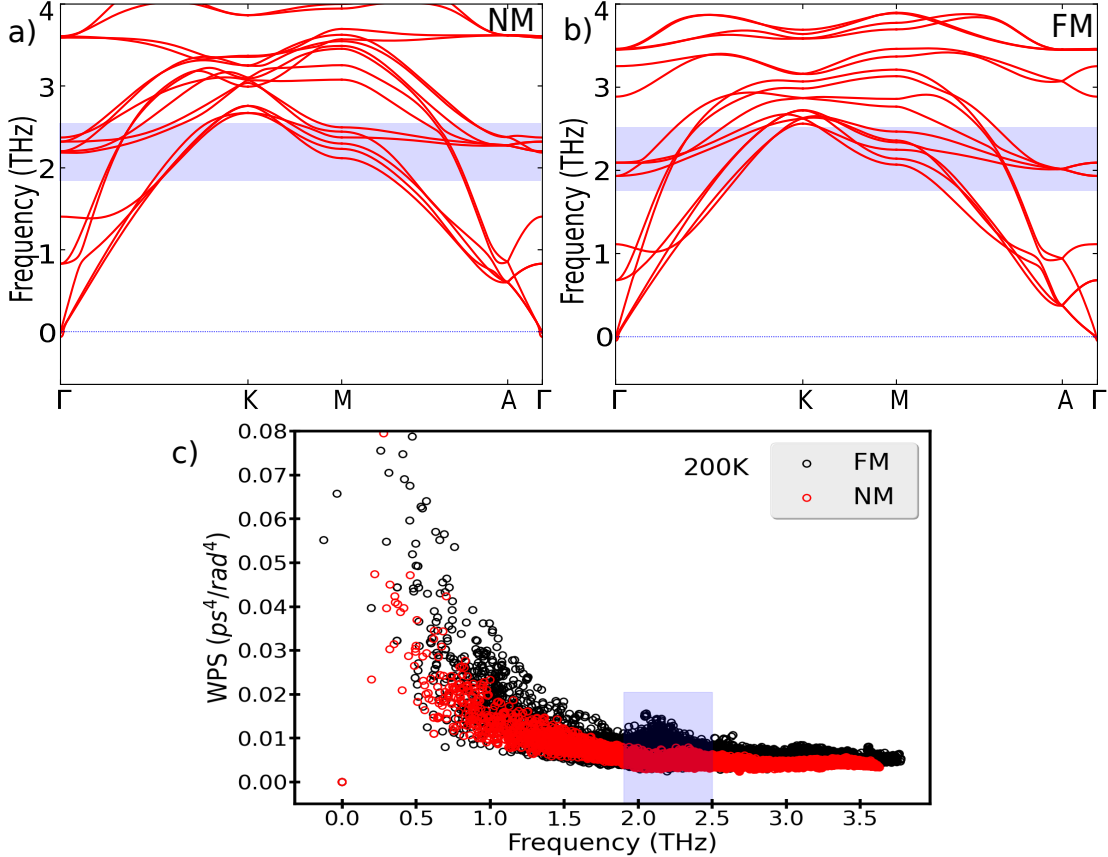


Figure 6: Phonon band diagrams for the magnetic (FM) a) and non magnetic (NM) b) ordering, and weighted phase space (WPS) available for three-phonon processes as a function of the frequency c). The shaded area in c) corresponds with the highlighted region in both band diagrams. The FM ordering shows an enhanced peak compared to the NM ordering in the WPS around 2.1 THz associated to Raman modes, leading to more scattering processes causing a reduction in the cross-plane thermal conductivity.

only a small change in the c-axis lattice parameter and thermal expansion, without any crystallographic transformation (Figure 2b).

In order to shed light on the observed experimental behavior, we have computed the temperature dependence of κ_{\perp} in the small-grain limit for the different experimental cases (Fig. 5b). The thickness of the flakes was used as the boundary length for the 41 nm and 22 nm flakes. For the superposition region, 22+41 nm, $\kappa_{\perp}^{22+41nm}$ was estimated considering that the two flakes of 22 and 41 nm act as two independent resistances in series $\kappa_{\perp}^{22+41nm} = \kappa_{\perp}^{22nm} \kappa_{\perp}^{41nm} / (\kappa_{\perp}^{22nm} + \kappa_{\perp}^{41nm})$. For temperatures above (below) T_C the non-

magnetic (NM) (ferromagnetic (FM) layers ordered antiferromagnetically) solution was considered when estimating the thermal conductivity. Our calculations show a $\approx 30\%$ drop in the thermal conductivity between the NM and FM phases in good agreement with the experimental observations. Note that the theoretical underestimation of the thermal conductivity is related to the limitations of the small-grain limit used in the calculations, in which the boundary scattering is overestimated, especially at higher temperatures and for larger samples. However, all the qualitative features are well captured on it.

To understand the reduction of κ_{\perp} when entering the magnetic phase we can analyze the phonon band structures and the weighted phase space (WPS) available for three-phonon processes for the non-magnetic and the ferromagnetic configurations (Fig. 6). This last quantity gives an idea of the frequencies involved in phonon scattering processes that are different in the FM and NM states. From the phonon band structures, we can observe that the acoustic phonons undergo a shift toward lower frequencies, especially in the A- Γ path. This is related to a decrease in group velocities in the out-of-plane direction and hence in the thermal conductivity³¹.

Moreover, the FM ordering shows an increase in the WPS, specifically a peak around 2 THz that is substantially different from the NM calculation. This peak is related to the phonon modes highlighted Fig. 6 a) and b) and corresponds to two E_{1g} Raman active modes. In the magnetic phase, these modes are about 0.3 THz lower in energy, showing more crossings with the acoustic modes. This results in additional scattering processes and causes a reduction in the thermal conductivity. The large coupling between Raman-active modes and a particular magnetic order has been reported in other two-dimensional magnets.³² Here, we observe that this results, together with the decrease in the group velocities of the acoustic modes, in a reduction of the lattice thermal conductivity in the magnetic phase.

Conclusion

To summarize, we have combined experimental FDTR and ab initio calculations to demonstrate that the cross-plane thermal conductivity of 2D ferromagnet FGT presents a mixed contribution of diffusive and ballistic phonons. We have also shown that κ_{\perp} presents an abrupt reduction below the Curie temperature, due to additional phonon scattering produced by a downshift in the frequency of acoustic and Raman-active optical phonons in the magnetic phase. Finally, artificial stacking of a few-layer thick FGT is a very useful way of reducing the cross-plane thermal conductivity in this material.

Experimental and Computational Details

Thermal conductivity was measured by Frequency Domain Thermoreflectance (FDTR)²⁰, using a 435 nm pump laser (1 mW) and a 532 nm probe laser (3 mW), respectively. A 60 nm gold thin film deposited by sputtering works as a reflective transducer. The fitting model considers Fourier heat conduction: the heat flux $q = -\kappa\nabla T$ where κ is a tensor to account for the material thermal conductivity anisotropy. The sample temperature is controlled inside a cold-finger optical cryostat, down to 80 K. The whole stage is mounted on a piezoelectric table which allows μm precision location of the laser spots on the sample. To promote the adhesion of FGT to the sapphire substrate, the samples were annealed under vacuum at 100°C before the experiments.

κ_{\perp} in the magnetic and non-magnetic phases of bulk FGT are calculated within a DFT^{33,34} framework using the VASP code.^{35–37} For all calculations, we have performed a full relaxation of the structure (both atomic positions and lattice parameters were optimized) with a mesh of $16 \times 16 \times 3$ k-points in the irreducible wedge of the Brillouin zone. The exchange-correlation potential chosen was the generalized gradient approximation in the Perdew-Burke-Ernzerhof scheme.³⁸ The second order interatomic force constants (IFCs) were determined using the Phonopy code^{39,40} in a $2 \times 2 \times 2$ supercell with a k-mesh of $8 \times 8 \times 2$ with

no further relaxation of cell shape or volume. Third order anharmonic IFCs were computed using the machinery of the ShengBTE code,⁴¹ considering interactions to third neighbors in a $2\times 2\times 2$ supercell. The lattice thermal conductivity was calculated by solving the Boltzmann Transport Equation (BTE) for phonons by an iterative self-consistent method implemented in the ShengBTE code within a mesh of $36\times 36\times 8$ q -points and a scalebroad parameter of 0.1.

Acknowledgement

This work has received financial support from Ministerio de Economía y Competitividad (Spain), projects PID2019-104150RB-I00 and PID2021-122609NB-C22, Xunta de Galicia (Centro singular de investigación de Galicia accreditation 2019-2022, ED431G 2019/03), the European Union (European Regional Development Fund-ERDF). We thank the CESGA (Centro de Supercomputación de Galicia for the computational facilities. A.O.F. acknowledges the Academy of Finland Project No. 349696.

Supporting Information Available

Additional figures with X-ray powder diffraction pattern of exfoliated crystal, FTDR sensitivity analysis and details of FDTR measurements with magnetic field.

References

1. Novoselov, K. S.; Geim, A. K.; Morozov, S. V.; Jiang, D.; Zhang, Y.; Dubonos, S. V.; Grigorieva, I. V.; Firsov, A. A. Electric Field Effect in Atomically Thin Carbon Films. *Science* **2004**, *306*, 666–669.
2. Novoselov, K. S.; Geim, A. K.; Morozov, S. V.; Jiang, D.; Katsnelson, M. I.; Grig-

orieva, I. V.; Dubonos, S. V.; Firsov, A. A. Two-dimensional gas of massless Dirac fermions in graphene. *Nature* **2005**, *438*, 197–200.

3. Novoselov, K. S.; Jiang, D.; Schedin, F.; Booth, T. J.; Khotkevich, V. V.; Morozov, S. V.; Geim, A. K. Two-dimensional atomic crystals. *Proceedings of the National Academy of Sciences* **2005**, *102*, 10451–10453.

4. Novoselov, K. S.; Mishchenko, A.; Carvalho, A.; Castro Neto, A. H. 2D materials and van der Waals heterostructures. *Science* **2016**, *353*, aac9439.

5. Jiang, P.; Qian, X.; Yang, R.; Lindsay, L. Anisotropic thermal transport in bulk hexagonal boron nitride. *Phys. Rev. Mater.* **2018**, *2*, 064005.

6. Sood, A.; Xiong, F.; Chen, S.; Cheaito, R.; Lian, F.; Asheghi, M.; Cui, Y.; Donadio, D.; Goodson, K. E.; Pop, E. Quasi-Ballistic Thermal Transport Across MoS₂ Thin Films. *Nano Letters* **2019**, *19*, 2434–2442.

7. Vakulov, D.; Gireesan, S.; Swinkels, M. Y.; Chavez, R.; Vogelaar, T.; Torres, P.; Campo, A.; De Luca, M.; Verheijen, M. A.; Koelling, S.; Gagliano, L.; Haverkort, J. E. M.; Alvarez, F. X.; Bobbert, P. A.; Zardo, I.; Bakkers, E. P. A. M. Ballistic Phonons in Ultrathin Nanowires. *Nano Letters* **2020**, *20*, 2703–2709.

8. Kim, S. E.; Mujid, F.; Rai, A.; Eriksson, F.; Suh, J.; Poddar, P.; Ray, A.; Park, C.; Fransson, E.; Zhong, Y.; Muller, D. A.; Erhart, P.; Cahill, D. G.; Park, J. Extremely anisotropic van der Waals thermal conductors. *Nature* **2021**, *597*, 660–665.

9. Deng, Y.; Yu, Y.; Song, Y.; Zhang, J.; Wang, N. Z.; Sun, Z.; Yi, Y.; Wu, Y. Z.; Wu, S.; Zhu, J.; Wang, J.; Chen, X. H.; Zhang, Y. Gate-tunable room-temperature ferromagnetism in two-dimensional Fe₃GeTe₂. *Nature* **2018**, *563*, 94.

10. Du, L.; Tang, J.; Zhao, Y.; Li, X.; Yang, R.; Hu, X.; Bai, X.; Wang, X.; Watanabe, K.; Taniguchi, T.; Shi, D.; Yu, G.; Bai, X.; Hasan, T.; Zhang, G.; Sun, Z. Lattice Dynamics,

Phonon Chirality, and Spin–Phonon Coupling in 2D Itinerant Ferromagnet Fe₃GeTe₂. *Advanced Functional Materials* **2019**, *29*, 1904734.

11. Wu, C.; Zhao, Y.; Zhang, G.; Liu, C. Giant thermal switching in ferromagnetic VSe₂ with programmable switching temperature. *Nanoscale Horizons* **2023**, *8*, 202–210.
12. Qin, G.; Wang, H.; Zhang, L.; Qin, Z.; Hu, M. Giant effect of spin–lattice coupling on the thermal transport in two-dimensional ferromagnetic CrI₃. *Journal of Materials Chemistry C* **2020**, *8*, 3520–3526.
13. Zhao, X.; Wu, J. C.; Zhao, Z. Y.; He, Z. Z.; Song, J. D.; Zhao, J. Y.; Liu, X. G.; Sun, X. F.; Li, X. G. Heat switch effect in an antiferromagnetic insulator Co₃V₂O₈. *Applied Physics Letters* **2016**, *108*, 242405.
14. Liu, Y.; Liu, Q.; Liu, Y.; Jiang, X.; Zhang, X.; Zhao, J. Effects of spin–phonon coupling on two-dimensional ferromagnetic semiconductors: a case study of iron and ruthenium trihalides. *Nanoscale* **2021**, *13*, 7714–7722.
15. Fei, Z.; Huang, B.; Malinowski, P.; Wang, W.; Song, T.; Sanchez, J.; Yao, W.; Xiao, D.; Zhu, X.; May, A. F.; Wu, W.; Cobden, D. H.; Chu, J.-H.; Xu, X. Two-dimensional itinerant ferromagnetism in atomically thin Fe₃GeTe₂. *Nature Materials* **2018**, *17*, 778–782.
16. May, A. F.; Calder, S.; Cantoni, C.; Cao, H.; McGuire, M. A. Magnetic structure and phase stability of the van der Waals bonded ferromagnet Fe_{3-x}GeTe₂. *Phys. Rev. B* **2016**, *93*, 014411.
17. Yi, J.; Zhuang, H.; Zou, Q.; Wu, Z.; Cao, G.; Tang, S.; Calder, S. A.; Kent, P. R. C.; Mandrus, D.; Gai, Z. Competing antiferromagnetism in a quasi-2D itinerant ferromagnet: Fe₃GeTe₂. *2D Materials* **2016**, *4*, 011005.

18. Spirito, D.; Barra-Burillo, M.; Calavalle, F.; Manganelli, C. L.; Gobbi, M.; Hillenbrand, R.; Casanova, F.; Hueso, L. E.; Martín-García, B. Tailoring Photoluminescence by Strain-Engineering in Layered Perovskite Flakes. *Nano Letters* **2022**, *22*, 4153–4160.

19. Tan, C.; Lee, J. L.; Jung, S.-G.; Park, T.; Albarakati, S.; Partridge, J.; R. Field, M.; G. McCulloch, D.; Wang, L.; Lee, C. Hard magnetic properties in nanoflake van der Waals Fe₃GeTe₂. *Nature Communications* **2018**, *9*, 1554, Number: 1.

20. Yang, J.; Maragliano, C.; Schmidt, A. J. Thermal property microscopy with frequency domain thermoreflectance. *Review of Scientific Instruments* **2013**, *84*, 104904, Publisher: American Institute of Physics.

21. Schmidt, A. J.; Cheaito, R.; Chiesa, M. A frequency-domain thermoreflectance method for the characterization of thermal properties. *Review of Scientific Instruments* **2009**, *80*, 094901, Publisher: American Institute of Physics.

22. Liu, Y.; Li, J.; Tao, J.; Zhu, Y.; Petrovic, C. Anisotropic magnetocaloric effect in Fe₃-xGeTe₂. *Scientific Reports* **2019**, *9*, 13233.

23. Langenberg, E.; Ferreiro-Vila, E.; Leborán, V.; Fumega, A. O.; Pardo, V.; Rivadulla, F. Analysis of the temperature dependence of the thermal conductivity of insulating single crystal oxides. *APL Materials* **2016**, *4*, 104815.

24. Zheng, W.; McClellan, C. J.; Pop, E.; Koh, Y. K. Nonequilibrium Phonon Thermal Resistance at MoS₂ /Oxide and Graphene/Oxide Interfaces. *ACS Applied Materials & Interfaces* **2022**, *14*, 22372–22380.

25. Xiao, P.; Chavez-Angel, E.; Chaitoglou, S.; Sledzinska, M.; Dimoulas, A.; Sotomayor Torres, C. M.; El Sachat, A. Anisotropic Thermal Conductivity of Crystalline Layered SnSe₂. *Nano Letters* **2021**, *21*, 9172–9179, PMID: 34710326.

26. Li, D.; Gao, J.; Cheng, P.; He, J.; Yin, Y.; Hu, Y.; Chen, L.; Cheng, Y.; Zhao, J. 2D boron sheets: structure, growth, and electronic and thermal transport properties. *Advanced Functional Materials* **2020**, *30*, 1904349.

27. Vaziri, S.; Yalon, E.; Muñoz Rojo, M.; Suryavanshi, S. V.; Zhang, H.; McClellan, C. J.; Bailey, C. S.; Smithe, K. K. H.; Gabourie, A. J.; Chen, V.; Deshmukh, S.; Bendersky, L.; Davydov, A. V.; Pop, E. Ultrahigh thermal isolation across heterogeneously layered two-dimensional materials. *Science Advances* **2019**, *5*, eaax1325.

28. Huang, H.-T.; Lai, M.-F.; Hou, Y.-F.; Wei, Z.-H. Influence of Magnetic Domain Walls and Magnetic Field on the Thermal Conductivity of Magnetic Nanowires. *Nano Letters* **2015**, *15*, 2773–2779.

29. Nakayama, H.; Xu, B.; Iwamoto, S.; Yamamoto, K.; Iguchi, R.; Miura, A.; Hirai, T.; Miura, Y.; Sakuraba, Y.; Shiomi, J.; Uchida, K.-i. Above-room-temperature giant thermal conductivity switching in spintronic multilayers. *Applied Physics Letters* **2021**, *118*, 042409.

30. Birch, M. T.; Powalla, L.; Wintz, S.; Hovorka, O.; Litzius, K.; Loudon, J. C.; Turnbull, L. A.; Nehruji, V.; Son, K.; Bubeck, C.; Rauch, T. G.; Weigand, M.; Goering, E.; Burghard, M.; Schütz, G. History-dependent domain and skyrmion formation in 2D van der Waals magnet Fe₃GeTe₂. *Nature Communications* **2022**, *13*, 3035, Number: 1.

31. Fumega, A. O.; Fu, Y.; Pardo, V.; Singh, D. J. Understanding the lattice thermal conductivity of SrTiO₃ from an ab initio perspective. *Phys. Rev. Mater.* **2020**, *4*, 033606.

32. Huang, B.; Cenker, J.; Zhang, X.; Ray, E. L.; Song, T.; Taniguchi, T.; Watanabe, K.; McGuire, M. A.; Xiao, D.; Xu, X. Tuning inelastic light scattering via symmetry control in the two-dimensional magnet CrI₃. *Nature nanotechnology* **2020**, *15*, 212–216.

33. Hohenberg, P.; Kohn, W. Inhomogeneous electron gas. *Physical review* **1964**, *136*, B864.

34. Kohn, W.; Sham, L. J. Self-consistent equations including exchange and correlation effects. *Physical review* **1965**, *140*, A1133.
35. Kresse, G.; Hafner, J. Ab initio molecular dynamics for liquid metals. *Physical review B* **1993**, *47*, 558.
36. Kresse, G.; Furthmüller, J. Efficiency of ab-initio total energy calculations for metals and semiconductors using a plane-wave basis set. *Computational materials science* **1996**, *6*, 15–50.
37. Kresse, G.; Furthmüller, J. Efficient iterative schemes for ab initio total-energy calculations using a plane-wave basis set. *Physical review B* **1996**, *54*, 11169.
38. Perdew, J. P.; Burke, K.; Ernzerhof, M. Generalized Gradient Approximation Made Simple. *Phys. Rev. Lett.* **1996**, *77*, 3865–3868.
39. Togo, A.; Tanaka, I. First principles phonon calculations in materials science. *Scr. Mater.* **2015**, *108*, 1–5.
40. Togo, A. First-principles Phonon Calculations with Phonopy and Phono3py. *J. Phys. Soc. Jpn.* **2023**, *92*, 012001.
41. Li, W.; Carrete, J.; Katcho, N. A.; Mingo, N. ShengBTE: a solver of the Boltzmann transport equation for phonons. *Comp. Phys. Commun.* **2014**, *185*, 1747–1758.

Supplementary information of

Temperature and thickness dependence of the thermal conductivity in 2D ferromagnet Fe_3GeTe_2

M. S. Claro,¹ J. Corral-Sertal,¹ A. Otero-Fumega,² S. Blanco-Canosa,^{3, 4} M. Suárez-Rodríguez,⁵ L. Hueso,^{5, 4} V. Pardo,^{6, 7} and F. Rivadulla¹

¹)CiQUS, Centro Singular de Investigacion en Quimica Bioloxica e Materiais Moleculares, Departamento de Quimica-Fisica, Universidade de Santiago de Compostela, 15782-Santiago de Compostela, Spain.

²)Department of Applied Physics, Aalto University, FI-00076 Aalto, Finland

³)Donostia International Physics Center (DIPC), 20018 San Sebastián, Spain

⁴)IKERBASQUE, Basque Foundation for Science, 48013 Bilbao, Spain

⁵)CIC nanoGUNE BRTA, Donostia-San Sebastián, Spain

⁶)Departamento de Física Aplicada, Universidade de Santiago de Compostela, E-15782 Santiago de Compostela, Spain

⁷)Instituto de Materiais iMATUS, Universidade de Santiago de Compostela, E-15782 Campus Sur s/n, Santiago de Compostela, Spain

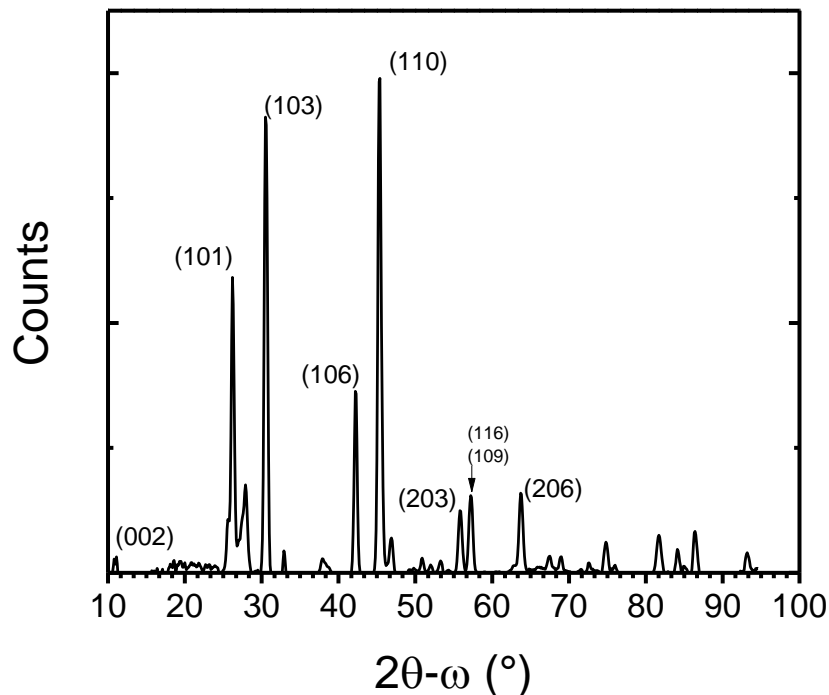


Figure S1. X-ray powder diffraction pattern with main crystallographic planes identified from the Fe_3GeTe_2 crystals used.

We define the sensitivity of the fitting parameter α as the logarithmic derivative of the FDTR phase-shift (ϕ) with respect to the parameter. If that parameter is set as α , then:

$$S_\alpha = \frac{d \phi}{d \ln \alpha}$$

The sensitivity for the parameters of interest (k , $G1$ and $G2$) is higher between 1 MHz to 50 MHz, the range used in the fittings.

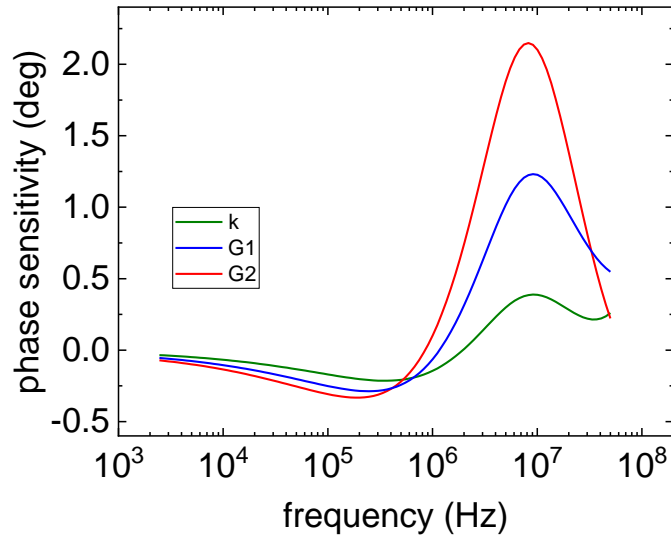


Figure S2. Phase sensitivity of out-of-plane thermal conductivity of Fe_3GeTe_2 (k), $G1$ and $G2$ TBCs in the Frequency Domain Thermoreflectance (FDTR) experiment.

Due to the strong correlation between the $G1$ and $G2$ parameters, in practice, only the sum $G1+G2$ is considered in the fitting. Figure S3 shows the variation of this parameter with temperature. These values were applied in the fitting presented in Figure 5a.

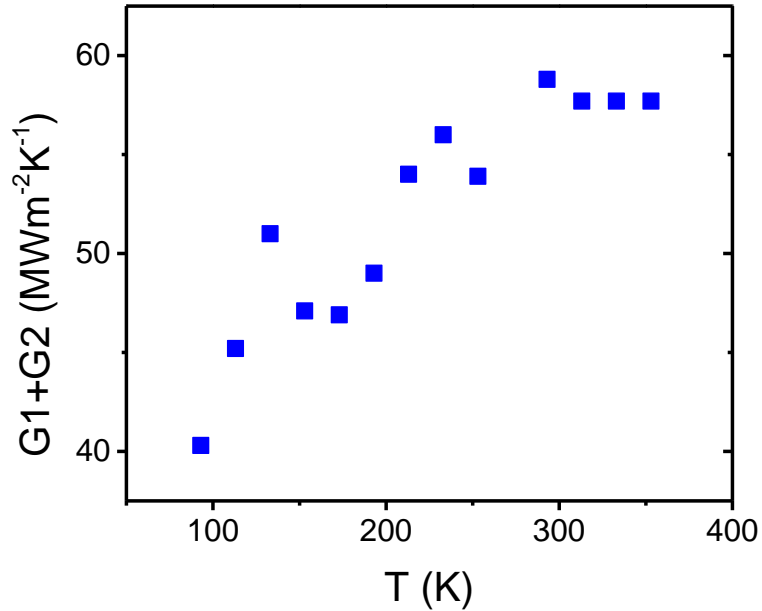


Figure S3. Total thermal boundary conductivity (TBC) G1+G2 TBCs extracted from the FTDR phase-shift fittings.

To apply an external magnetic field to the thin films, we have used permanent magnets made of NdFeB (N45). These magnets can be placed and removed keeping the measured spot fixed.

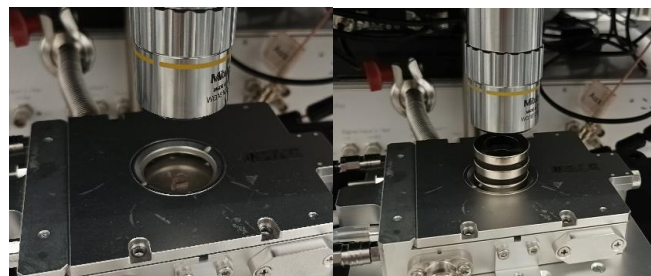


Figure S4. Sample inside the optical cryostat below the FDTR confocal lenses (left) and added toroidal magnets for measurements with a magnetic field (right).

The toroidal shape allows the transmission of the pump and probe laser without any interference. Moreover, this shape creates a considerably uniform and constant out-of-plane magnetic field. Since

magnetization and geometry are well known, the field was determined using Finite Element Method (FEMM 4.2) (Figure S5) from which we estimate a field of 56 mT in the sample plane.

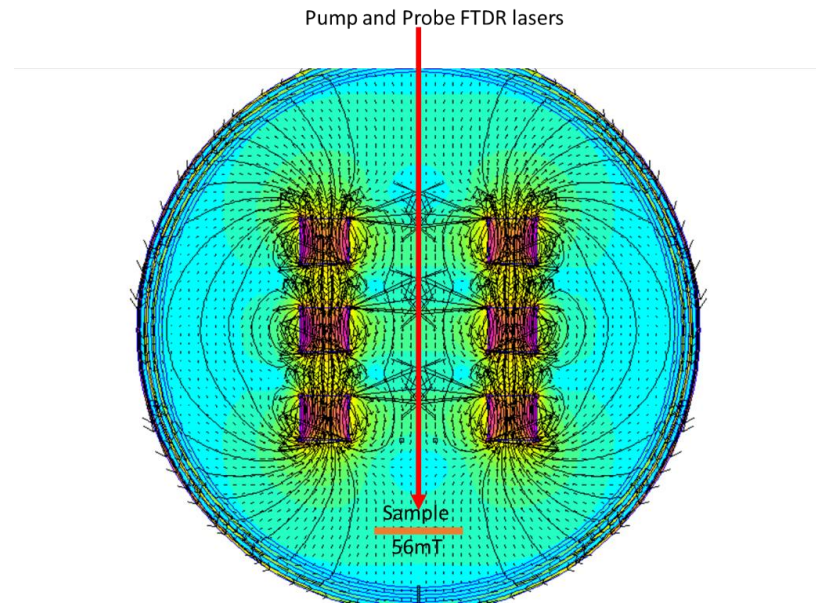


Figure S5. Finite-Element (FEM) simulation of the Magnetic Field applied to the sample during the FDTR experiment with toroidal permanent magnets.